An Al–Al interpenetrating-phase composite by 3D printing and hot extrusion

Yulin Lin, Di Wang, Chao Yang, Weiwen Zhang, and Zhi Wang

View the article online at SpringerLink or IJMMM Webpage.

Articles you may be interested in

Yi-wa Luo, Ming-yong Wang, Ji-guo Tu, Yu Jiang, and Shu-qiang Jiao, Reduction of residual stress in porous Ti6Al4V by *in situ* double scanning during laser additive manufacturing, *Int. J. Miner. Metall. Mater.*, 28(2021), No. 11, pp. 1844-1853. https://doi.org/10.1007/s12613-020-2212-z

Li Zhang, Bao-lin Wu, and Yu-lin Liu, Microstructure and mechanical properties of a hot-extruded Al-based composite reinforced with core-shell-structured Ti/Al$_3$Ti, *Int. J. Miner. Metall. Mater.*, 24(2017), No. 12, pp. 1431-1437. https://doi.org/10.1007/s12613-017-1536-9

Hong-yu Chen, Dong-dong Gu, Qing Ge, Xin-yu Shi, Hong-mei Zhang, Rui Wang, Han Zhang, and Konrad Kosiba, Role of laser scan strategies in defect control, microstructural evolution and mechanical properties of steel matrix composites prepared by laser additive manufacturing, *Int. J. Miner. Metall. Mater.*, 28(2021), No. 3, pp. 462-474. https://doi.org/10.1007/s12613-020-2133-x

Y. Pazhuhanfar and B. Eghbali, Processing and characterization of the microstructure and mechanical properties of Al6061–TiB$_2$ composite, *Int. J. Miner. Metall. Mater.*, 28(2021), No. 6, pp. 1080-1089. https://doi.org/10.1007/s12613-021-2288-0

Yu-ting Wu, Chong Li, Ye-fan Li, Jing Wu, Xing-chuan Xia, and Yong-chang Liu, Effects of heat treatment on the microstructure and mechanical properties of Ni$_3$Al-based superalloys: A review, *Int. J. Miner. Metall. Mater.*, 28(2021), No. 4, pp. 553-566. https://doi.org/10.1007/s12613-020-2177-y

Yi-li Dai, Sheng-fu Yu, An-guo Huang, and Yu-sheng Shi, Microstructure and mechanical properties of high-strength low alloy steel by wire and arc additive manufacturing, *Int. J. Miner. Metall. Mater.*, 27(2020), No. 7, pp. 933-942. https://doi.org/10.1007/s12613-019-1919-1

IJMMM WeChat   QQ author group

An Al–Al interpenetrating-phase composite by 3D printing and hot extrusion

Yulin Lin[1,2], *Di Wang*[1),✉], *Chao Yang*[1,2], *Weiwen Zhang*[1,2], *and Zhi Wang*[1,2),✉]

1) School of Mechanical and Automotive Engineering, South China University of Technology, Guangzhou 510640, China
2) Guangdong Key Laboratory for Processing and Forming of Advanced Metallic Materials, South China University of Technology, Guangzhou 510640, China

Abstract: We report a process route to fabricate an Al–Al interpenetrating-phase composite by combining the Al–Mg–Mn–Sc–Zr lattice structure and $Al_{84}Ni_7Gd_6Co_3$ nanostructured structure. The lattice structure was produced by the selective laser melting and subsequently filled with the $Al_{84}Ni_7Gd_6Co_3$ amorphous powder, and finally the mixture was used for hot extrusion to produce bulk samples. The results show that the composites achieve a high densification and good interface bonding due to the element diffusion and plastic deformation during hot extrusion. The bulk samples show a heterogeneous structure with a combination of honeycomb lattice structure with an average grain size of less than 1 μm and nanostructured area with a high volume fraction of nanometric intermetallics and nanograin α-Al. The heterogeneous structure leads to a bimodal mechanical zone with hard area and soft area giving rise to high strength and acceptable plasticity, where the compressive yield strength and the compressive plasticity can reach ~745 MPa and ~30%, respectively. The high strength can be explained by the rule of mixture, the grain boundary strengthening, and the back stress, while the acceptable plasticity is mainly owing to the confinement effect of the nanostructured area retarding the brittle fracture behavior.

Keywords: Al-based composites; heterogeneous structure; additive manufacturing; mechanical properties

1. Introduction

Al-based composites have been considered as ideal materials for important lightweight structural parts because of their low density, high strength, and good corrosion resistance [1–2]. In the past few decades, a variety of Al-based composites have been developed by using ceramic particles, glass fibers, graphene, and carbon nanotubes as reinforcement phases, showing improved strength, hardness, and wear properties [3–6]. Nevertheless, there is an urgent need for designing new composite structures to obtain optimized mechanical properties such as good ductility and shock energy absorption properties.

Recently hierarchical structure and/or interpenetrating-phase materials have been well developed owing to their better balance between the strength and ductility. For example, the hierarchical structure can give rise to high strain harden ability leading to high uniform plastic deform [7–10]. Complex lattice structures can be produced by additive manufacturing (AM) processes, e.g., additive manufactured Al alloys have been widely developed, showing high design flexibility and complex geometry for the components [11]. In particularly, Al–Mg–Mn–Sc–Zr alloys have been found having good additive manufacturing ability and showing high strength and reasonable ductility [12–14]. Meanwhile the nanostructured Al alloys show super high strength but limited ductility. For example, Wang *et al.* [15] prepared an

$Al_{84}Ni_7Gd_6Co_3$ nanostructured Al alloy with a compressive yield strength as high as 1700 MPa. Therefore, the high strength nanostructured Al alloy can be further used to strengthen the selective laser melted (SLMed) Al–Mg–Mn–Sc–Zr alloy, on the other hand, the SLMed Al–Mg–Mn–Sc–Zr alloy lattice structure can restrict the brittle fracture behavior of the nanostructured alloy.

In this work, we designed a novel Al-based composite with interpenetrating-phase structure, in which an Al–Mg–Mn–Sc–Zr alloy lattice structure with honeycomb shape was produced by SLM process and the holes of the lattice structure were filled with the $Al_{84}Ni_7Gd_6Co_3$ nanostructured Al alloy by hot extrusion. The microstructure and mechanical properties were studied.

2. Experimental

The powders with a nominal composition $Al_{84}Ni_7Gd_6Co_3$ (at%) and Al–Mg–Mn–Sc–Zr were produced by argon-gas atomization method (shown in Fig. 1(a) and (b)), which have a particle size range of 20–63 and 0–53 μm, respectively. The chemical composition of the Al–Mg–Mn–Sc–Zr powder is listed in Table 1. The as-atomized $Al_{84}Ni_7Gd_6Co_3$ powder particles with diameters larger than 5 μm display the presence of partial crystalline precipitates (Fig. 1(b)), suggesting partially crystallization occurred. A regular hexagonal honeycomb structure with 1 mm wall thickness, 14 mm diamet-
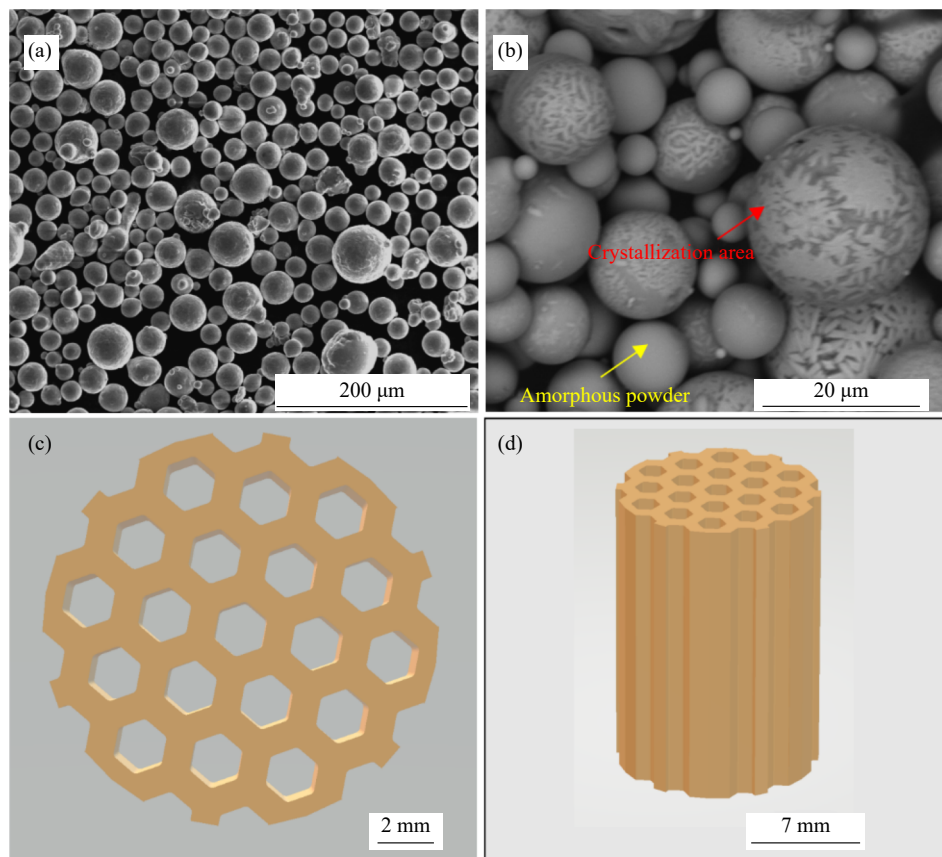
Springer

Fig. 1. Morphology of the powders and lattice structure: (a, b) SEM images of the Al–Mg–Mn–Sc–Zr and the $Al_{84}Ni_7Gd_6Co_3$ powders; (c, d) lattice model.

Table 1. Chemical composition of the Al–Mg–Mn–Sc–Zr powders   wt%

Mg	Mn	Sc	Zr	Si	Al
4.76	0.58	0.47	0.29	0.05	Bal.

er, and 30 mm height was prepared by using a selective laser melting equipment (Dimetal-100H, South China University of Technology, China). The SLM process parameters are: laser power 150 W, scanning speed 400 mm/s, scanning spacing 0.08 mm, layer thickness 0.03 mm, and rotation angle of each layer 67°. Fig. 2 schematically showed the preparation process of the composite. The honeycomb lattice structures were pretreated by abrasive flow to improve the surface quality and then filled with the $Al_{84}Ni_7Gd_6Co_3$ alloy powders by mechanical vibration and subsequently consolidated into bulk composite samples by cold pressing and hot extrusion. The hot extrusion pressure and extrusion ratio were chosen at a fixed value of 590 MPa and 10, respectively. The hot extrusion temperature for composites was chosen at 573, 673, and 773 K, respectively (marked as Composite A, Composite B, and Composite C, respectively, as shown in Table 2). The final samples in the form of cylindrical billet have a diameter of ~5 mm and a length of ~135 mm. In addition, the monolithic SLMed Al–Mg–Mn–Sc–Zr alloy and the monolithic $Al_{84}Ni_7Gd_6Co_3$ alloy were processed by hot extrusion at the same pressure, extrusion ratio, and temperature of 573 K.

The samples for microstructural observation were etched by Keller's reagent with a composition of 1 mL HF, 1.5 mL HCL, 2.5 mL HNO_3, and 95 mL distilled water for ~25 s. The microstructure was observed with a German Leica DMI5000M optical microscope (OM), Quanta200 scanning electron microscope (SEM) equipped with a HKL-Technology electron backscattered diffraction (EBSD) detection system, and Philips Tecnai F30 transmission electron microscope (TEM) operating at 300 kV with an energy dispersive X-ray (EDS). The crystallographic data were characterized by EBSD. After mechanical polishing, the samples for EBSD were revealed using an electrolytic polishing solution with a composition of 30vol% HNO_3 and 70vol% methanol and the voltage was 25 V for 30 s. Scanning step size of 0.06 μm was used for the EBSD analysis. Phase composition was studied by X-ray diffraction (XRD) using a Germany Bruker D8-Adavancec machine with Co K radiation at a step size of 0.025° and a counting time of 1 s per step. The internal defects of the samples were analyzed using Germany dinodo d2 3D X-ray computed tomography (3D-CT) machine. The microhardness (HV) was measured using a HVS-1000 microhardness tester with a load of 300 g and dwell time of 10 s. The microhardness values reported here are the averages of >6 indentations per sample. According to ASTM compression test standard, cylindrical specimens with a height of 6 mm and a diameter of 3 mm were prepared. Uniaxial compressive tests were performed at room temperature using a CMT5105 microcomputer controlled electronic universal testing machine at a constant strain rate of 1×10^{-3} s^{-1} and at
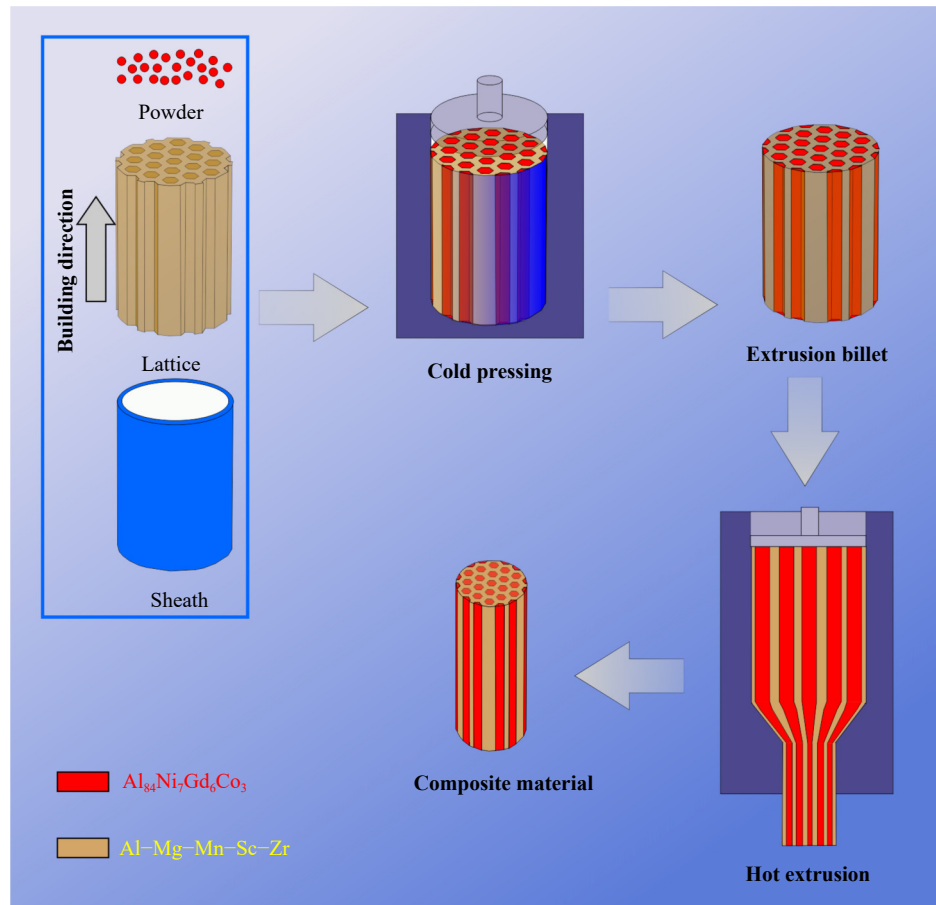
Fig. 2. Schematic illustration of the preparation process for the composites with lattice structure.

Table 2. Hot extrusion processing parameters

Material	Pressure / MPa	Holding time / min	Extrusion ratio	Temperature / K
Composite A	590	30	10	573
Composite B	590	30	10	673
Composite C	590	30	10	773

least three samples were tested for each material.

3. Results and discussion

3.1. Microstructure

Fig. 3(a) and (b) shows the microstructure of the as-built lattice structure, showing the laser scanning tracks intersecting with each other, which is similar with the reported SLMed Al–Mg–Sc–Zr alloy [16]. The black line and the bright area show the edge area and the interior of the molten pool track, respectively. It is shown that the edge area and interior area of the molten pool track is mainly composed of fine grains and column grains, respectively, which is similar with the reported works [17–18]. Fig. 3(c) and (d) shows the transverse sectional OM image and longitudinal sectional 3D-CT image of the Composite A, respectively. They indicate that the honeycomb lattice structure was preserved without significant torsion and bending after hot extrusion. In addition, no cracks are observed in the interface between the honeycomb lattice structure and the $Al_{84}Ni_7Gd_6Co_3$ alloy

area. The $Al_{84}Ni_7Gd_6Co_3$ alloy area shows nanostructure which is similar with our previous reported works [15]. For simplicity, here we call the honeycomb lattice structure area (SLMed Al–Mg–Mn–Sc–Zr alloy area) and the $Al_{84}Ni_7Gd_6Co_3$ alloy area as lattice area and nanostructured area, respectively. Fig. 3(f) shows the densification behaviour of the Composite A, showing that the porosity is 0.0024% with pores and micro-cracks. The pores show an average diameter of ~1 μm and are homogeneously distributed in the whole sample. The microcracks are mainly concentrated in the nanostructured area (as shown in Fig. 3(d) and (f)) with average length and average width of 126 and 1 μm, respectively. The microcracks occurred in the nanostructured area are owing to the high volume fraction of brittle intermetallics (as high as 80vol%) [19]. The brittle intermetallics were contacted each other during hot extrusion and gave rise to high local stress, initiating cracks.

Fig. 4 shows the morphology of the lattice area in the composites. As shown in Fig. 4(a) and (b), the molten pool and laser scanning track formed from the SLM process was clearly seen in the lattice area, which were elongated along extrusion direction. As shown in Fig. 4(a–f), the molten pool tracks became weak with the increasing extrusion temperature since the homogenization was accelerated at high temperatures.

Fig. 5 shows the X-ray diffraction results of the composites. The fine precipitates in the lattice structure area are difficult to distinguish from the XRD patterns owing to their low
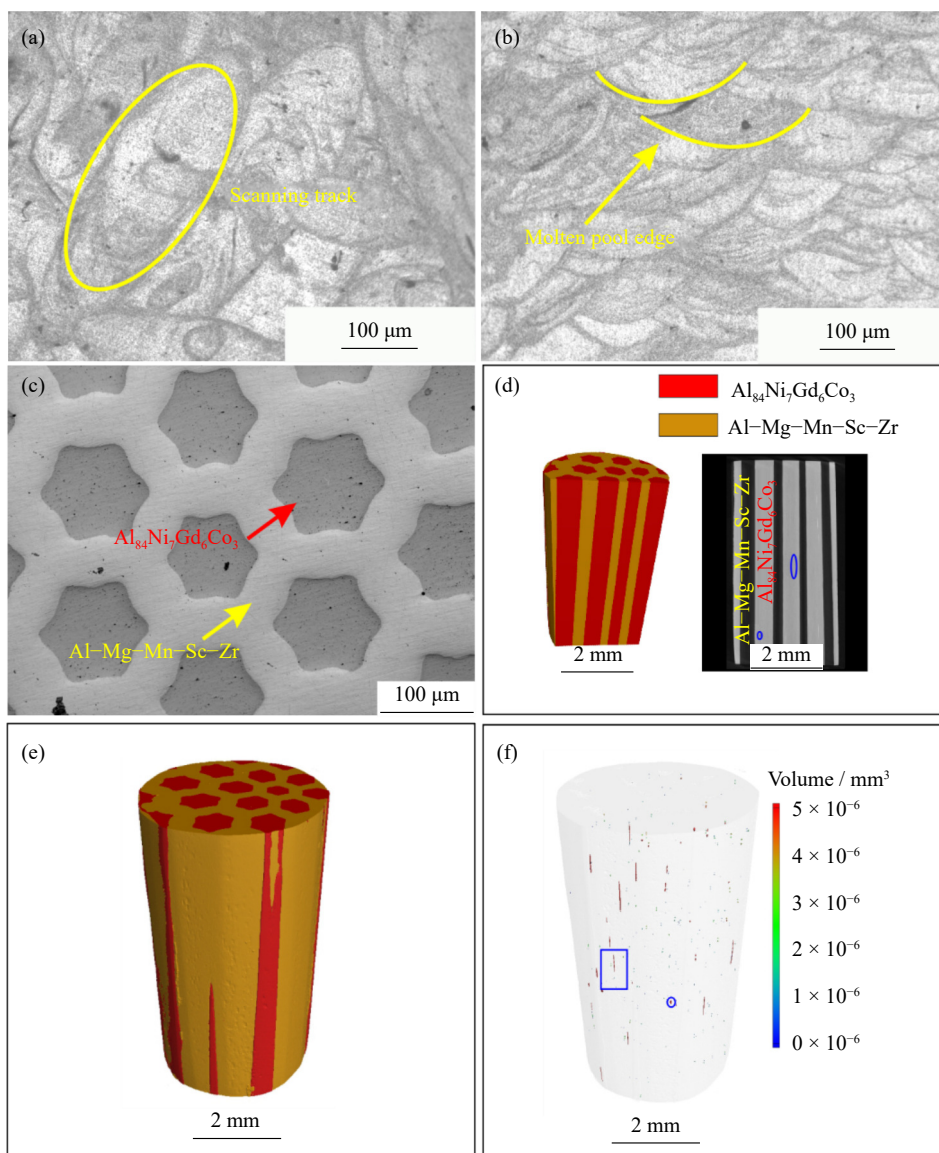
Fig. 3. (a, b) Transverse sectional and longitudinal sectional optical micrograph of the as-built lattice structure; (c) transverse sectional optical micrograph of the Composite A after polishing; (d) longitudinal sectional 3D-CT image of Composite A; (e) 3D-CT reconstruction of Composite A; (f) densification behaviour evaluation of Composite A by 3D-CT analysis.

volume faction. The amorphous $Al_{84}Ni_7Gd_6Co_3$ powders are found *in-situ* crystallized into α-Al and intermetallics such as Al_9Co_2, Al_3Gd, and $Al_{19}Gd_3Ni_5$, which is similar to our previous reported works [15,20–21]. The intensity of intermetallics peaks increases with increasing hot extrusion temperature, indicating that high temperatures promoted the transformation of amorphous regions into intermetallics. It is found that a high volume fraction of intermetallics existed in the composites.

Fig. 6 shows electron back scattering images of the longitudinal sectional interface of the composites. It shows metallurgical bonding without microcracks and pores, which is mostly owing to the element diffusion and plastic deformation during hot extrusion. Different from the heterogeneous materials fabricated by casting [22], the plastic deformation during hot extrusion make the composites more compacted. Due to the extremely small size of phases, elemental analysis in nanostructured area was carried out by TEM–EDS utiliz-

ing elemental point analysis (Fig. 6(i)), with the results listed in Table 3. The nanostructured area in the Composite C exhibits hybrid structures consisting of nanometric rod-like phases, equiaxed particle-like phases, and α-Al. The α-Al has a grain size of ~80 nm, and the nanometric intermetallics have an average of 100–250 nm in the fine precipitate region. The size of these phases in the coarse precipitate region reaches ~3 μm. The size of the intermetallics decreases with the decrease of extrusion temperature. On the other hand, different precipitates are observed in the lattice area. Due to the high cooling rate in the SLM process and lower extrusion temperature, the size of the precipitates in the lattice area in Composite A is very small. Similar to the growth of nanostructured regions, the size of the precipitates increases with the increase of extrusion temperature. Large Mn-rich phase particles and small Sc-rich phase particles were found through energy spectrum plane scanning results.

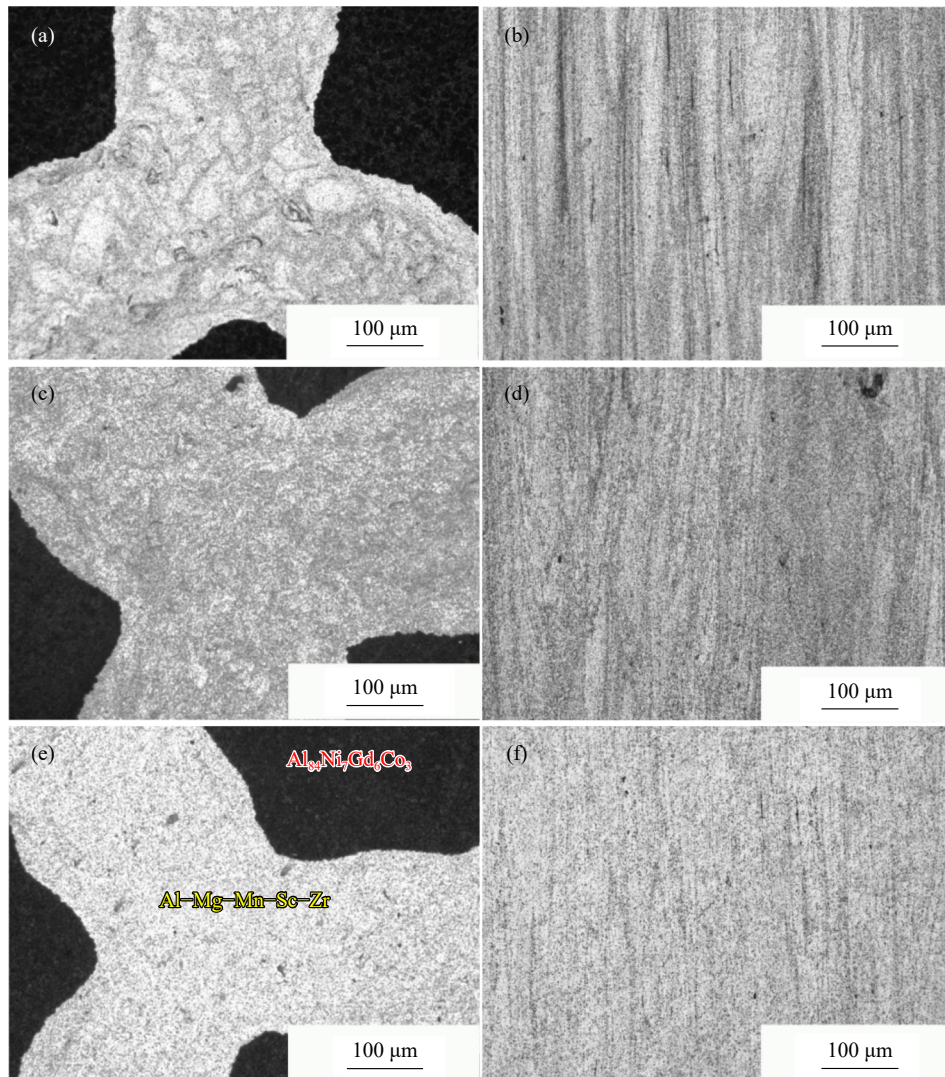Fig. 7 shows the EBSD and grain size distribution dia-

Fig. 4. (a, c, e) Transverse sectional OM of the lattice area in the Composites A, Composites B, and Composites C, respectively; (b, d, f) longitudinal sectional OM of lattice structures in the Composites A, Composites B, and Composites C, respectively.
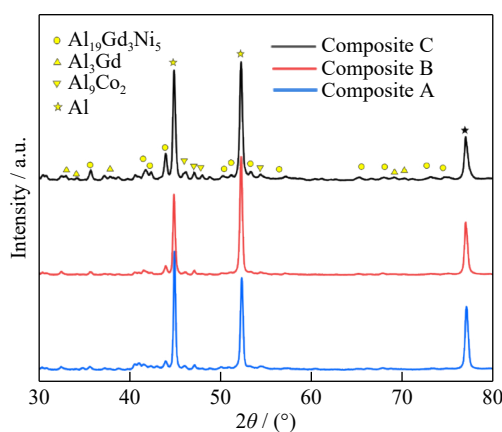

Fig. 5. XRD patterns of the composites.

gram of the lattice area in different composites. After hot extrusion, the lattice area shows different grain morphology consisting of fine equiaxed grains (FEGs) and long elongated grains (LEGs). The FEGs with a fine grain size of ~1 μm are distributed throughout the sample, indicating that they are derived from the fine equiaxed grain zone at the edge of the

molten pool track formed during SLM. The LEGs with aspect ratio of more than 10 and length of ~20 μm are formed by the plastic deformation of the columnar grain zone in the interior of the molten pool. The average grain size of lattice area in Composite A, Composite B, and Composite C are 0.79, 0.91, and 0.70 μm, respectively. It proves that the grains of the lattice area undergo partially recrystallization, resulting into the formation of fine and equiaxed grain. The remained non-recrystallization grains are found to form fiber textures of <100> and <111> along the extrusion direction.

3.2. Mechanical behavior

Fig. 8(a) shows the microhardness of the different regions in the composites at different extrusion temperatures. The microhardness of the lattice areas and nanostructured areas decreases with the increase of extrusion temperature, and the microhardness of nanostructured areas decreases faster than that of lattice areas. It is seen from Fig. 8(b) that the hardness of the interface decreases gradually with the increase of extrusion temperature. When the extrusion temperature is 573 K, the microhardness difference between the nanostructure
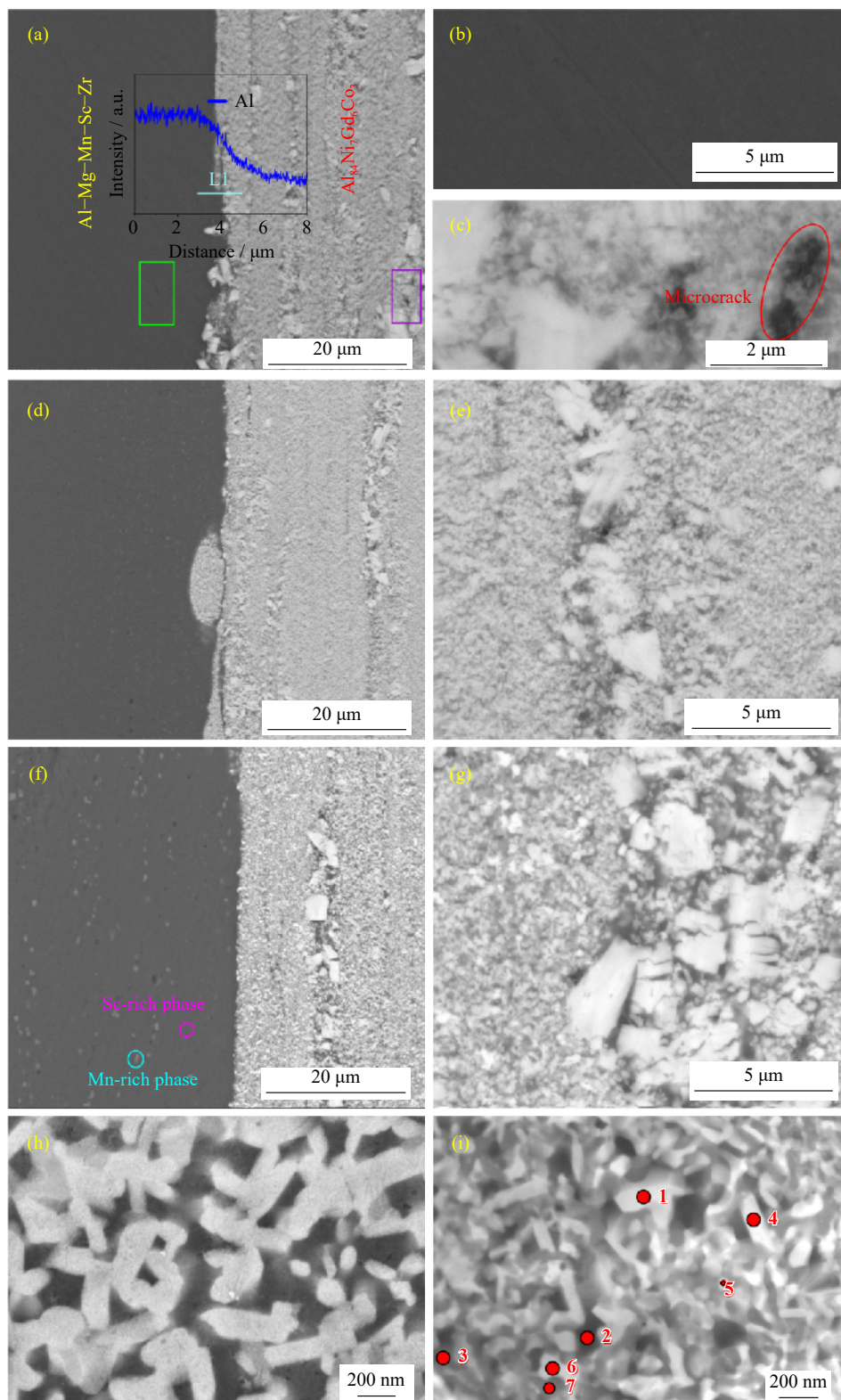
Fig. 6. Electron back scattering images of longitudinal section in the different composites and TEM of fine precipitate region in nanostructured area of Composite C: (a) interface of Composite A and energy spectrum line scan, (d) interface of Composite B and (f) Composite C; (b, c) high resolution images of different regions in Composite A, (e) nanostructured area of Composite B and (g) Composite C; (h) high resolution SEM image of the nanostructured area in Composite C; (i) TEM image of the nanostructured area in Composite C.

region and the lattice structure region is the largest. The decrease of microhardness in the nanostructured area is owing to the coarsening of intermetallics, and the decrease of microhardness in the lattice region is resulted from the grain

coarsening, recrystallization, and precipitates coarsening.

Typical room temperature stress–strain curves under uniaxial compressive quasistatic loading are shown in Fig. 9(a). The monolithic hot extruded $Al_{84}Ni_7Gd_6Co_3$ alloy shows a

Table 3.   Element contents in Fig. 6(i) measured via TEM–EDS

Location	Al / at%	Ni / at%	Gd / at%	Co / at%
Point 1	Bal.	0.38	30.21	2.21
Point 2	Bal.	0	0	0
Point 3	Bal.	20.11	3.37	7.74
Point 4	Bal.	18.28	15.52	6.03
Point 5	Bal.	9.03	13.92	4.78
Point 6	Bal.	1.01	27.36	3.11
Point 7	Bal.	14.62	0.18	7.72

yield strength of 1030 MPa with ~1% plasticity. The monolithic SLMed Al–Mg–Mn–Sc–Zr alloy shows a yield strength of 506 MPa and large compressive plasticity. The yield strength of the composites increases significantly comparing with the monolithic SLMed Al–Mg–Mn–Sc–Zr alloy, which is 745, 629, and 542 MPa for the Composite A, Composite B, and Composite C, respectively. In addition, the composites show acceptable compressive plasticity, e.g., Composite A shows a compressive plasticity of ~30%. It indicates that the compression stress of the lattice area has been improved remarkably by the nanostructured area. Strain
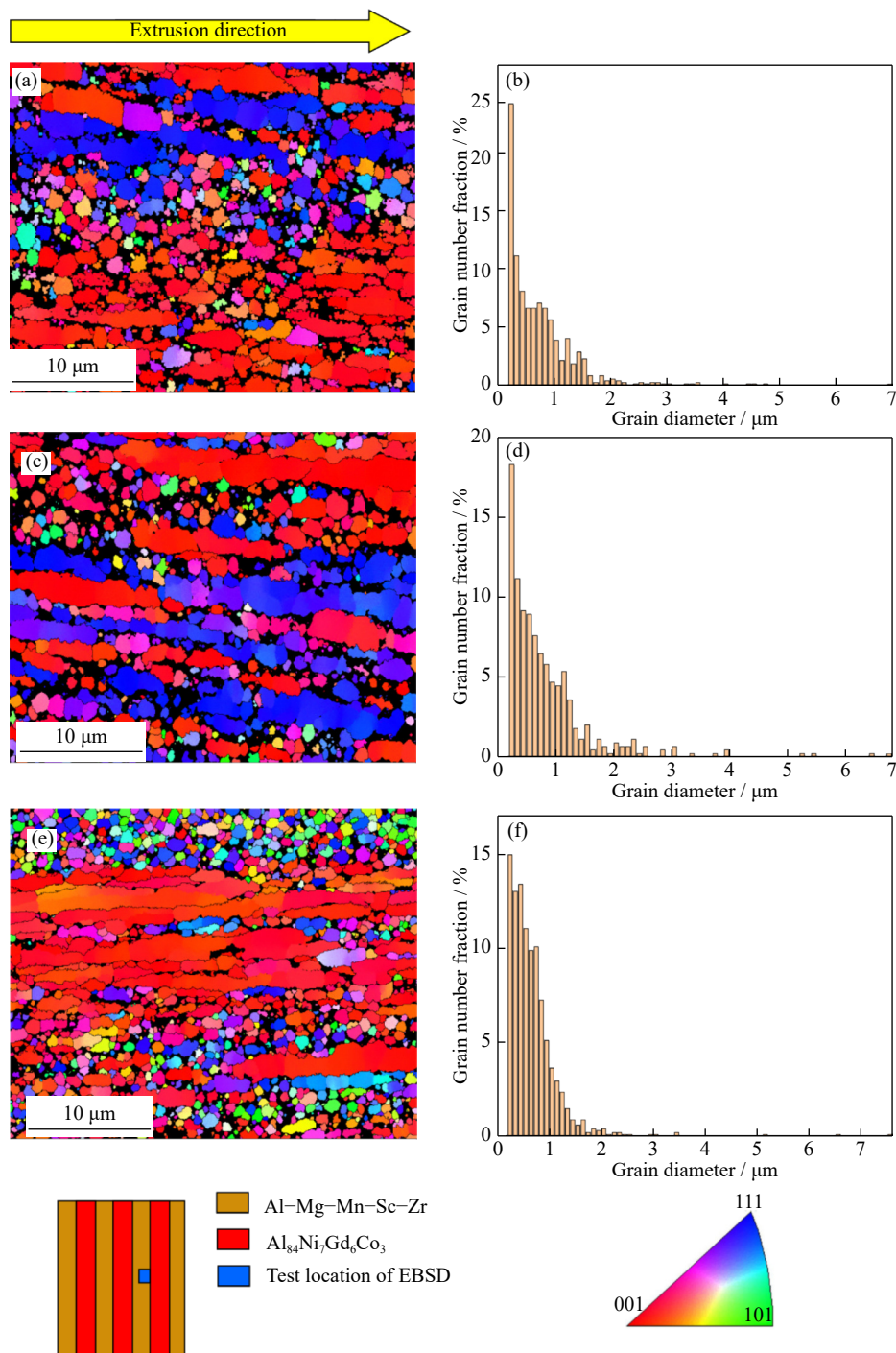

Fig. 7.   Inverse pole figure (IPF-X) mapping and grain size distribution of the lattice area in the different composites: (a, b) Composite A; (c, d) Composite B; (e, f) Composite C.
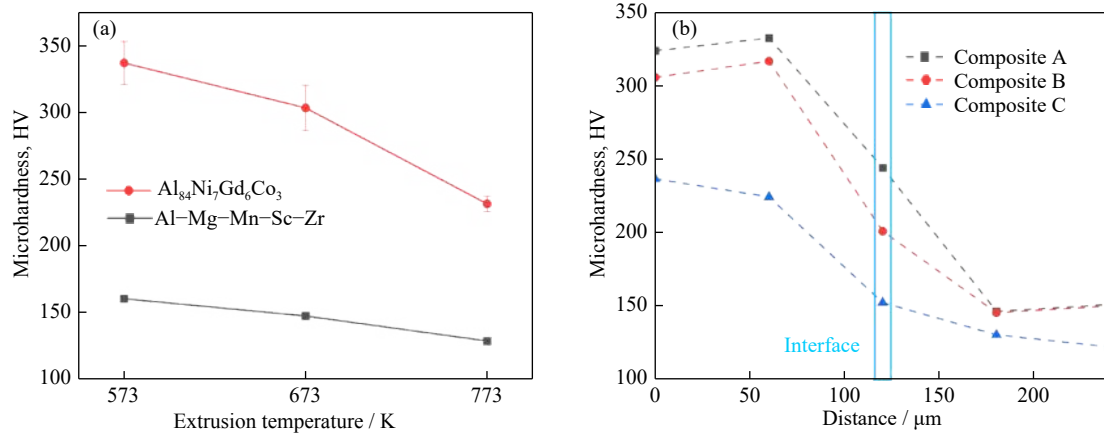
Fig. 8. (a) Vickers hardness of the composites produced at different extrusion temperatures and (b) Vickers hardness distribution in composites.
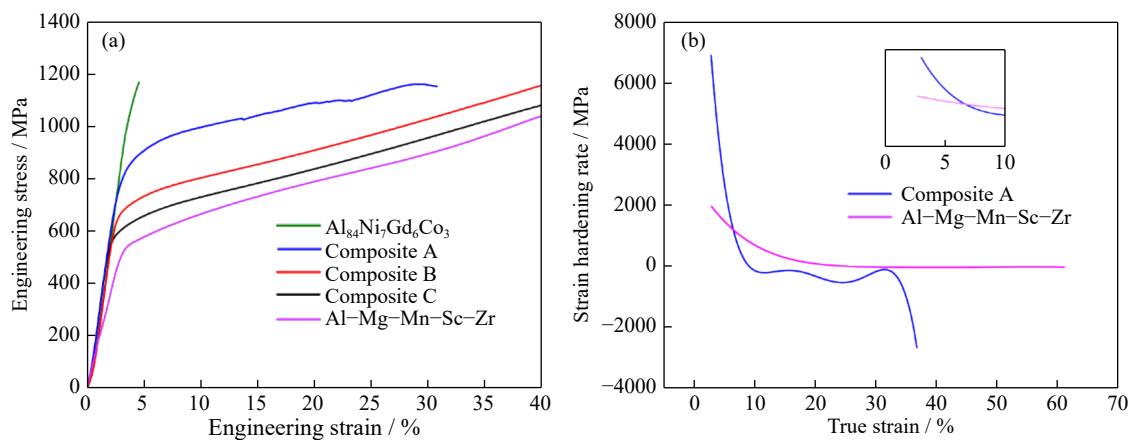

Fig. 9. (a) Compressive engineering stress–strain curves and (b) strain hardening rate as a function of true strain upon compression of Composite A and Al–Mg–Mn–Sc–Zr.

hardening rate curves are shown in Fig. 9(b), the work hardening rate of Composite A is higher than that of monolithic SLMed Al–Mg–Mn–Sc–Zr alloy in the early deformation process (true strain < 7%). With the progress of deformation, the work hardening rate of Composite A firstly decreases and then increases to a relatively high value, and finally decreases sharply when the material fractured. This phenomenon is similar to that of Al–Mg–Sc–Zr alloy with heterogeneous structure reported by Wang *et al.* [14], which is mostly related to back stress hardening. According to the 3D-CT measurement, the volume fraction of the nanostructured area in the Composite A is ~41vol%. From the rule of mixtures (ROM), the flow stress of the composites is calculated in its simplest form.

$$\sigma = \sigma_1 \times f_1 + \sigma_2 \times f_2 + \cdots + \sigma_n \times f_n \qquad (1)$$

where $\sigma_1, \sigma_2, \sigma_n$ are flow stress and f_1, f_2, f_n are volume fraction. The yield strength of the Composite A calculated from ROM is 720 MPa, which is smaller than the measured. According to the high work hardening rate during the early deformation process and the difference between the ROM value and the measured value of the Composite A, it indicates that there are other strengthening mechanisms.

Fig. 10 shows the 3D-CT micrographs of the Composite A after compressive deformation. It shows the interface de-

bonding was rarely occurred. During the compression deformation, the brittle behavior of the nanostructured area is confined by the lattice area. With further loading, microcracks were firstly initiated from the brittle nanostructured area and retarded by the interface. According to the Kolednik's crack arrest model [23], the crack driving force decreases rapidly as the crack enters the soft zone, which is consistent with the experimental results. When the local stress near the interface surpasses the yield strength of the lattice area, plastic deformation occurred, further leading to blunting effect for the crack propagation. Finally, when the local stress is higher than the fracture stress of the lattice area, the main crack was formed and propagated along the direction of the maximum tangential stress, eventually leading to the failure.

The high strength and acceptable plasticity of Composite A are mainly attributed to the unique heterogeneous structure constituting by nanostructured area with super high strength and lattice area with good plasticity. The nanostructured area shows super high strength which is mainly attributed to the high volume fraction of nanometric intermetallics. While the lattice area shows the combination of good plasticity and strength mainly arising from fine grain strengthening and precipitation hardening. According to the works by
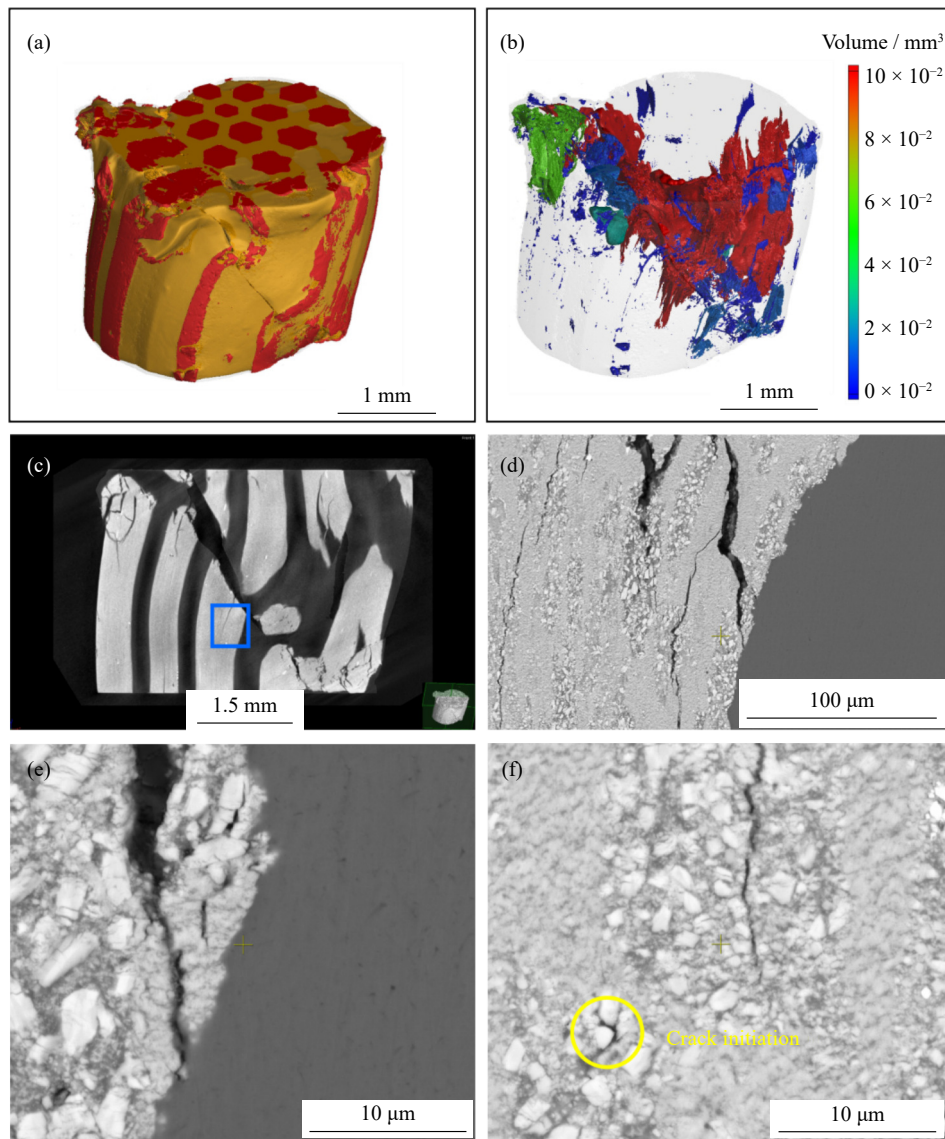
Fig. 10.   (a) 3D-CT image of Composite A reconstruction, (b) quantitative characterization of defects in Composite A after compression using 3D-CT, (c) longitudinal sectional 3D-CT image of Composite A, and (d) lower and (e, f) higher magnification longitudinal sectional fracture morphology of Composite A.

Geng *et al.* [24] and Ma *et al.* [25], the fine grains and $Al_3(Sc,Zr)$ particles formed after aging and plastic deformation of SLMed Al–Mg–Mn–Sc–Zr strongly hinder the dislocation movement. In addition, the nanostructured area is harder than the lattice area, leading to bimodal mechanical zone with hard zone and soft zone in the Composite A. Therefore, back stress strengthening was introduced near the interface of the composite giving high strength of the lattice area. This back stress strengthening has been well demonstrated in heterogeneous materials [7–10]. The introduction of back stress improves the strength and work hardening capacity of lattice structure and retards the crack propagation which is in turn improve the fracture stress. With the increase of extrusion temperature, both grain coarsening and recrystallization and precipitates coarsening occurred in the lattice area and intermetallics coarsening occurred in the nanostructured area, resulting in the strength decrease of the composites.

It has been demonstrated that high strength Al matrix give rise to confinement effect, limiting the premature fracture of

the brittle high strength materials [15,26–28],

$$(\sigma_1 - \sigma_3)^2 = 2(2 + \alpha^2)\tau_0^2 + 2\alpha^2\sigma_1\sigma_3 \tag{2}$$

where α is materials constant, τ_0 is critical shear fracture stress, σ_1 and σ_3 are the maximum and minimum principal stress, respectively. In compressive loading condition, $\sigma_1 + \sigma_3 < 0$. Since $\tau_{max} = (\sigma_1 - \sigma_3)/2$, one gets the effective shear yield stress:

$$\tau_y = \sqrt{\frac{(2 + \alpha^2)\tau_0^2}{2} + \frac{\alpha^2\sigma_1\sigma_3}{2}} \tag{3}$$

where $\sqrt{\sigma_1\sigma_3} \leq (\sigma_1 + \sigma_3)/2$, one can define $\sqrt{\sigma_1\sigma_3}$ as the confining stress to characterize the magnitude of confinement [15,26,29]. In this work, the Al–Mg–Mn–Sc–Zr lattice area retarded the crack initiation and propagation in the $Al_{84}Ni_7Gd_6Co_3$ nanostructured area, changing the fracture behavior of the nanostructured area from the main crack propagation to the development of dense and dispersed microcracks. Therefore, although microcracks occurred in the

nanostructured area, the composite can still carry the load, leading to the acceptable compressive plasticity.

4. Conclusions

In summary, a novel Al-based composite with interpenetrating-phase has been developed by fabricating Al–Mg–Mn–Sc–Zr lattice structure using SLM and filling with $Al_{84}Ni_7Gd_6Co_3$ powders, and further processed into bulk samples via hot extrusion. The following conclusions can be drawn.

(1) The composites show high densification and good interface bonding owing to the element diffusion and plastic deformation during hot extrusion. The honeycomb lattice structure did not bend significantly during hot extrusion.

(2) The heterogeneous structure shows a combination of a honeycomb lattice structure with an average grain size of less than 1 μm and nanostructured area with a high volume fraction of nanometric intermetallics and nanograin α-Al.

(3) The composite shows a bimodal mechanical zone with hard zone (nanostructured zone) and soft zone (lattice zone), leading to high strength and acceptable plasticity. The high strength can be explained by the rule of mixture, the grain boundary strengthening, and the back stress in the lattice structure area. The acceptable plasticity is mainly owing to the confinement effect of the nanostructured area by the lattice area.

Acknowledgements

Conflict of Interest

The authors declare no potential conflict of interest.

References

[1] Y. Mei, P.Z. Shao, M. Sun, *et al*., Deformation treatment and microstructure of graphene-reinforced metal matrix nanocomposites: A review of graphene post-dispersion, *Int. J. Miner. Metall. Mater.*, 27(2020), No. 7, p. 888.

[2] C.S. Kim, K. Cho, M.H. Manjili, and M. Nezafati, Mechanical performance of particulate-reinforced Al metal-matrix composites (MMCs) and Al metal-matrix nano-composites (MMNCs), *J. Mater. Sci*, 52(2017), No. 23, p. 13319.

[3] E. Safary, R. Taghiabadi, and M.H. Ghoncheh, Mechanical properties of Al–15Mg$_2$Si composites prepared under different solidification cooling rates, *Int. J. Miner. Metall. Mater.*, 29(2022), No. 6, p. 1249.

[4] Z. Wang, K. Georgarakis, K.S. Nakayama, *et al*., Microstruc-

ture and mechanical behavior of metallic glass fiber-reinforced Al alloy matrix composites, *Sci. Rep.*, 6(2016), art. No. 24384.

[5] M.C. Şenel, Y. Kanca, and M. Gürbüz, Reciprocating sliding wear properties of sintered Al–B$_4$C composites, *Int. J. Miner. Metall. Mater.*, 29(2022), No. 6, p. 1261.

[6] C. He, N. Zhao, C. Shi, *et al*., An approach to obtaining homogeneously dispersed carbon nanotubes in Al powders for preparing reinforced Al-matrix composites, *Adv. Mater.*, 19(2007), No. 8, p. 1128.

[7] X.L. Ma, C.X. Huang, J. Moering, *et al*., Mechanical properties of copper/bronze laminates: Role of interfaces, *Acta Mater.*, 116(2016), p. 43.

[8] X.C. Liu, Z. Liu, Y.J. Liu, *et al*., Achieving high strength and toughness by engineering 3D artificial nacre-like structures inTi$_6$Al$_4$V–Ti metallic composite, *Composites Part B*, 230(2022), art. No. 109552.

[9] M.Y. Zhang, Q. Yu, Z.Q. Liu, *et al*., 3D printed Mg–NiTi interpenetrating-phase composites with high strength, damping capacity, and energy absorption efficiency, *Sci. Adv.*, 6(2020), No. 19, art. No. eaba5581.

[10] C.W. Shao, S. Zhao, X.G. Wang, Y.K. Zhu, Z. F.Zhang, and R.O. Ritchie, Architecture of high-strength aluminum–matrix composites processed by a novel microcasting technique, *NPG Asia Mater.*, 11(2019), art. No. 69.

[11] T. Maconachie, M. Leary, B. Lozanovski, *et al*., SLM lattice structures: Properties, performance, applications and challenges, *Mater. Des.*, 183(2019), art. No. 108137.

[12] R.D. Li, H. Chen, H.B. Zhu, M.B. Wang, C. Chen, and T.C. Yuan, Effect of aging treatment on the microstructure and mechanical properties of Al–3.02Mg–0.2Sc–0.1Zr alloy printed by selective laser melting, *Mater. Des.*, 168(2019), art. No. 107668.

[13] R.D. Li, M.B. Wang, Z.M. Li, P. Cao, T.C. Yuan, and H.B. Zhu, Developing a high-strength Al–Mg–Si–Sc–Zr alloy for selective laser melting: Crack-inhibiting and multiple strengthening mechanisms, *Acta Mater.*, 193(2020), p. 83.

[14] Z.H. Wang, X. Lin, N. Kang, Y.L. Hu, J. Chen, and W.D. Huang, Strength-ductility synergy of selective laser melted Al–Mg–Sc–Zr alloy with a heterogeneous grain structure, *Addit. Manuf.*, 34(2020), art. No. 101260.

[15] Z. Wang, R.T. Qu, S. Scudino, *et al*., Hybrid nanostructured aluminum alloy with super-high strength, *NPG Asia Mater.*, 7(2015), No. 12, art. No. e229.

[16] R.L. Ma, C.Q. Peng, Z.Y. Cai, *et al*., Manipulating the microstructure and tensile properties of selective laser melted Al–Mg–Sc–Zr alloy through heat treatment, *J. Alloys Compd.*, 831(2020), art. No. 154773.

[17] J.H. Zhao, L.S. Luo, X. Xue, *et al*., The evolution and characterizations of Al$_3$(Sc$_x$Zr$_{1-x}$) phase in Al–Mg-based alloys proceeded by SLM, *Mater. Sci. Eng. A*, 824(2021), art. No. 141863.

[18] A. Spierings, K. Dawson, T. Heeling, *et al*., Microstructural features of Sc- and Zr-modified Al–Mg alloys processed by selective laser melting, *Mater. Des.*, 115(2017), p. 52.

[19] Z. Wang, K.G. Prashanth, S. Scudino, *et al*., Tensile properties of Al matrix composites reinforced with *in situ* devitrified Al$_{84}$Gd$_6$Ni$_7$Co$_3$ glassy particles, *J. Alloys Compd.*, 586(2014), p. S419.

[20] Z. Wang, K.G. Prashanth, S. Scudino, *et al*., Effect of ball milling on structure and thermal stability of Al$_{84}$Gd$_6$Ni$_7$Co$_3$ glassy powders, *Intermetallics*, 46(2014), p. 97.

[21] Z. Wang, K.G. Prashanth, K.B. Surreddi, C. Suryanarayana, J. Eckert, and S.Scudino, Pressure-assisted sintering of Al–Gd–Ni–Co amorphous alloy powders, *Materialia*, 2(2018), p. 157.

[22] A.E. Pawlowski, Z.C. Cordero, M.R. French, *et al*., Damage-tolerant metallic composites via melt infiltration of additively

688

Int. J. Miner. Metall. Mater., Vol. 30, No. 4, Apr. 2023

manufactured preforms, *Mater. Des.*, 127(2017), p. 346.

[23] O. Kolednik, J. Predan, F.D. Fischer, and P. Fratzl, Bioinspired design criteria for damage-resistant materials with periodically varying microstructure, *Adv. Funct. Mater.*, 21(2011), No. 19, p. 3634.

[24] Y.X. Geng, H. Tang, J.H. Xu, Z.J. Zhang, Y.K. Xiao, and Y. Wu, Strengthening mechanisms of high-performance Al–Mn–Mg–Sc–Zr alloy fabricated by selective laser melting, *Sci. China Mater.*, 64(2021), No. 12, p. 3131.

[25] R.L. Ma, C.Q. Peng, Z.Y. Cai, *et al*., Enhanced strength of the selective laser melted Al–Mg–Sc–Zr alloy by cold rolling, *Mater. Sci. Eng. A*, 775(2020), art. No. 138975.

[26] S.Y. Kim, G.Y. Lee, G.H. Park, *et al*., High strength nanostruc-tured Al-based alloys through optimized processing of rapidly quenched amorphous precursors, *Sci. Rep.*, 8(2018), No. 1, art. No. 1090.

[27] X.J. Shen, C. Zhang, Y.G. Yang, and L. Liu, On the microstruc-ture, mechanical properties and wear resistance of an additively manufactured Ti64/metallic glass composite, *Addit. Manuf.*, 25(2019), p. 499.

[28] Z. Tan, L. Wang, Y.F. Xue, *et al*., A multiple grain size distrib-uted Al-based composite consist of amorphous/nanocrystalline, submicron grain and micron grain fabricated through spark plasma sintering, *J. Alloys Compd.*, 737(2018), p. 308.

[29] R.T. Qu and Z.F. Zhang, A universal fracture criterion for high-strength materials, *Sci. Rep.*, 3(2013), art. No. 1117.